-Electronic Supplementary Information-

Solar production of fuels from CO_2 with high efficiency and stability via *in situ* transformation of Bi electrocatalyst

Woo Seok Cheon[a], Su Geun Ji[a,b], Jaehyun Kim[a], Sungkyun Choi[a], Jin Wook Yang[a], Sang Eon Jun[a], Changyeon Kim[a], Jeewon Bu[a], Sohyeon Park[a], Tae Hyung Lee[a], Jinghan Wang[a], Jae Young Kim[a], Sol A Lee[a,c], Jin Young Kim[a,], Ho Won Jang[a,d,]**

[a] Department of Materials Science and Engineering, Research Institute of Advanced Materials, Seoul National University, Seoul, 08826, Republic of Korea

[b] Chemistry and Nanoscience Center, National Renewable Energy Laboratory, Golden, Colorado 80401, United States

[c] Liquid Sunlight Alliance (LiSA), Department of Applied Physics and Materials Science, California Institute of Technology, Pasadena, CA, 91106 USA

[d] Advanced Institute of Convergence Technology, Seoul National University, Suwon 16229, Republic of Korea

*Correspondence: hwjang@snu.ac.kr, jykim.mse@snu.ac.kr

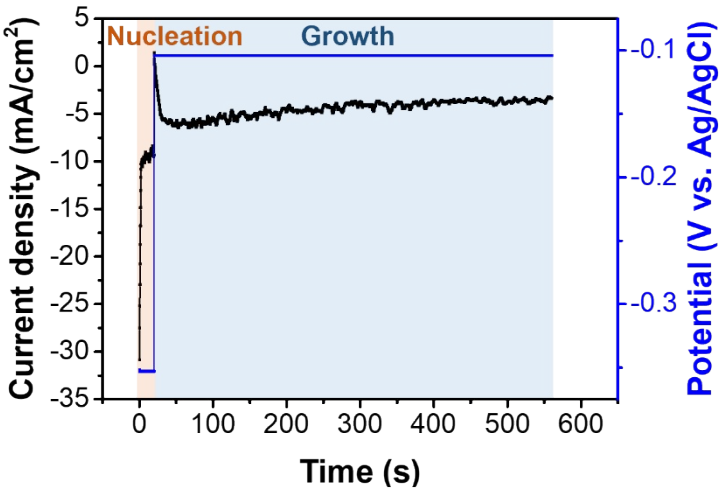

Figure S1. Two-step electrodeposition process of BiOI on carbon paper.

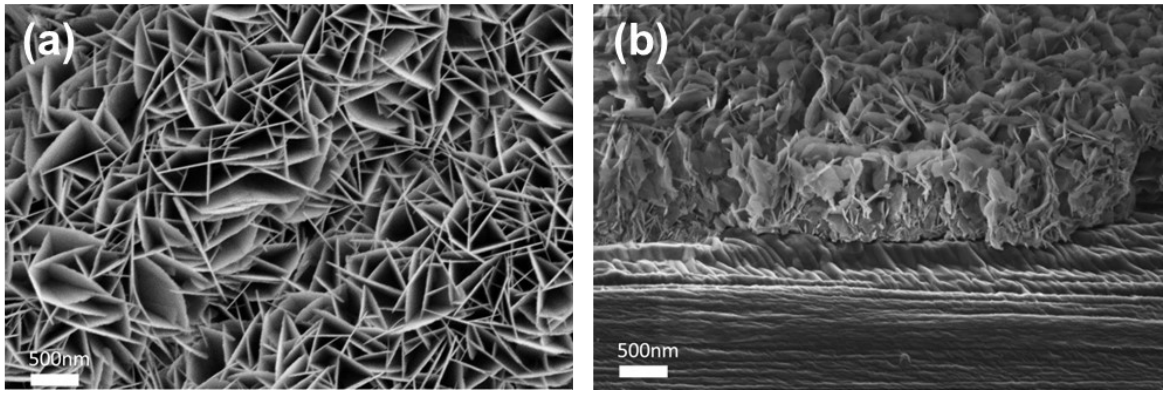

Figure S2. BiOI SEM images (a) top-view (b) cross-sectional view.

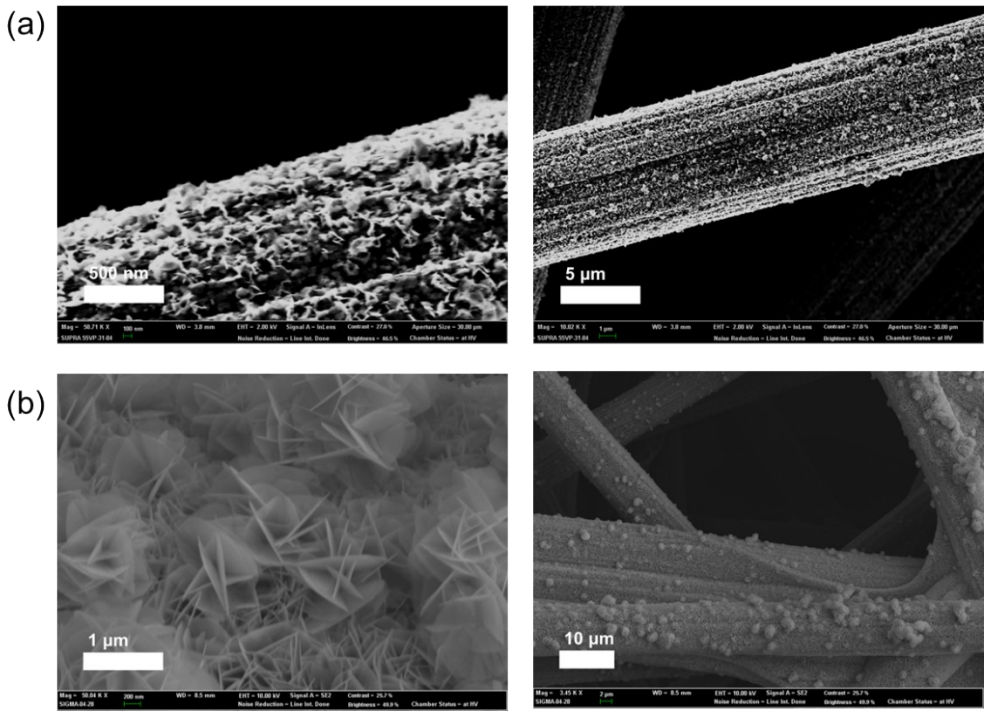

Figure S3. SEM images of BiOI with different electrodeposition time (a) 60 s (b) 720 s.

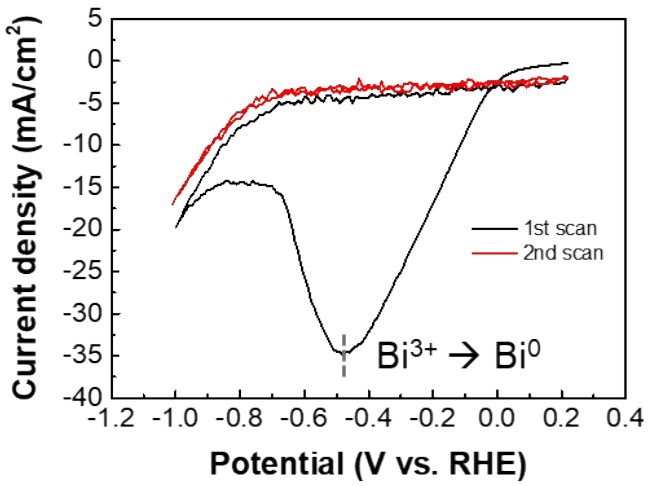

Figure S4. CV of BiOI in 0.2 M $KHCO_3$.

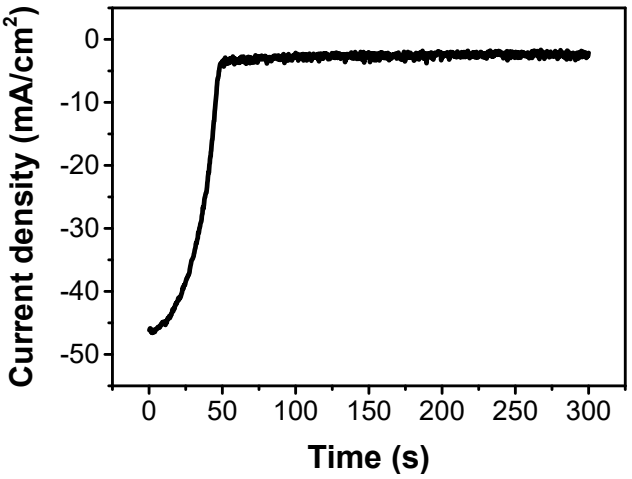

Figure S5. Chronoamperometric (CA) reduction of BiOI to Bi-VNS at -0.5 V_{RHE}.

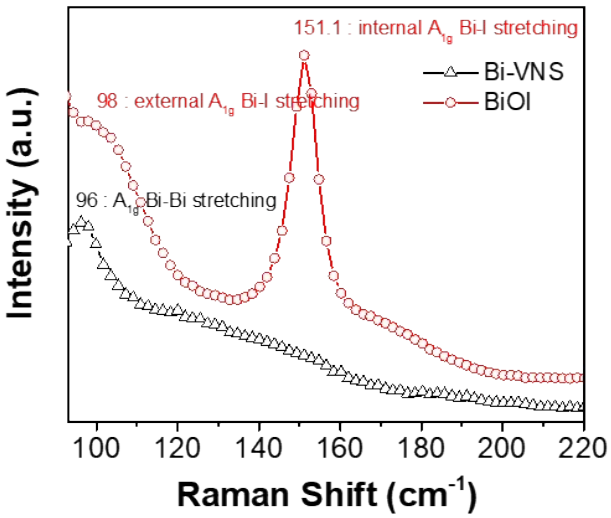

Figure S6. Raman spectra of BiOI and Bi-VNS

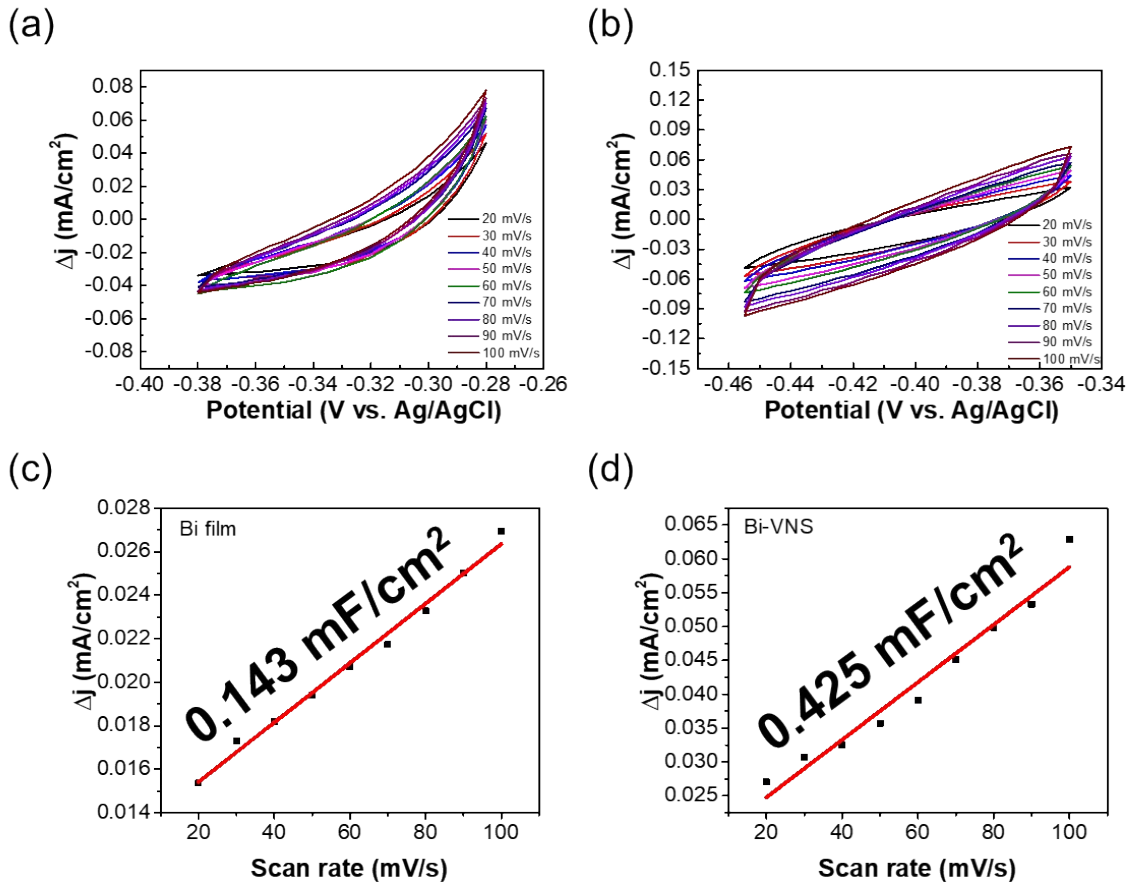

Figure S7. CV curves at different scan rates of (a) Bi film and (b) Bi-VNS. Calculated double-layer capacitances (C_{DL}) of (c) Bi film (d) Bi-VNS.

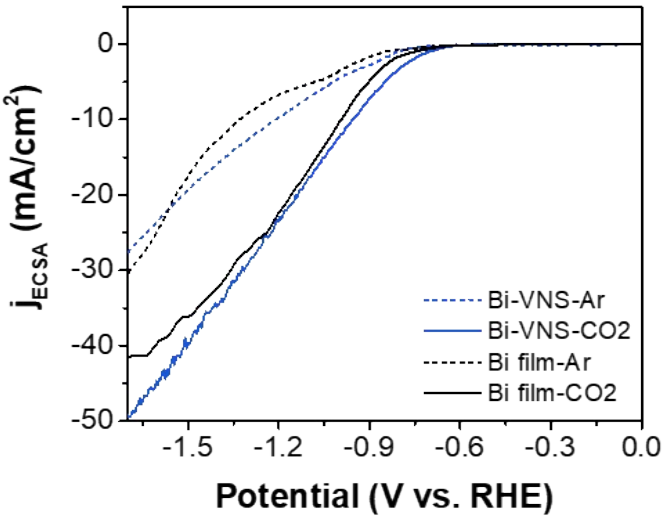

Figure S8. ECSA-normalized LSVs of Bi film and Bi-VNS

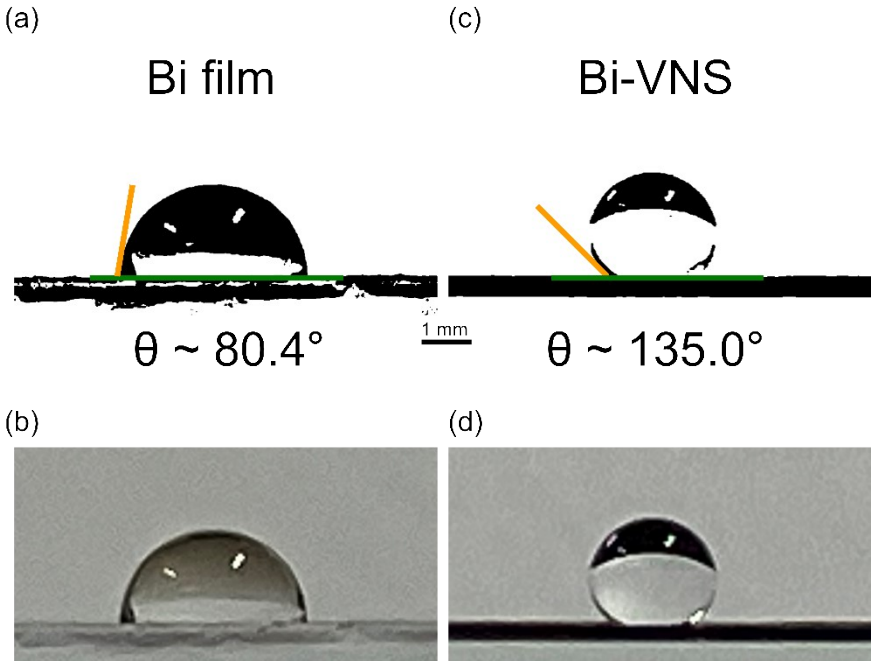

Figure S9. Contact angle measurement of water on (a, b) Bi film and (c, d) Bi-VNS

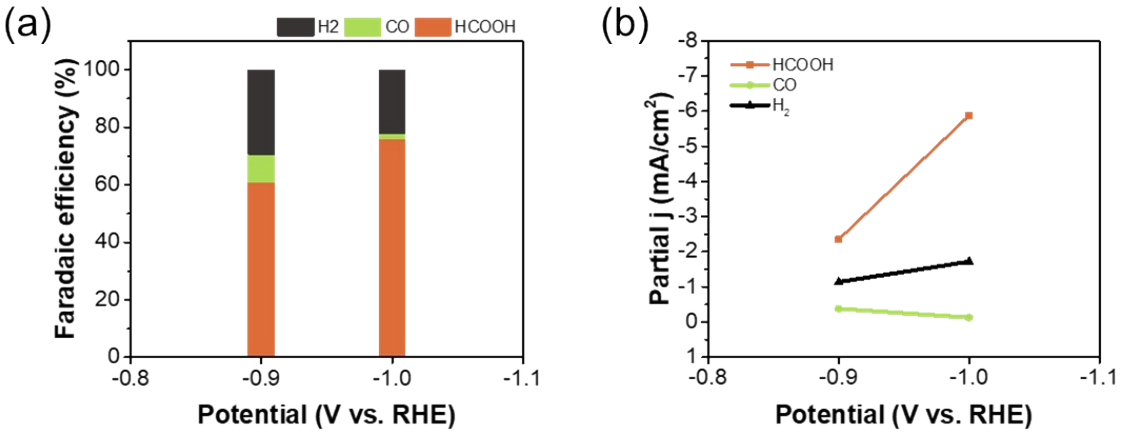

Figure S10. (a) FE and (b) j_{HCOOH} of Bi film.

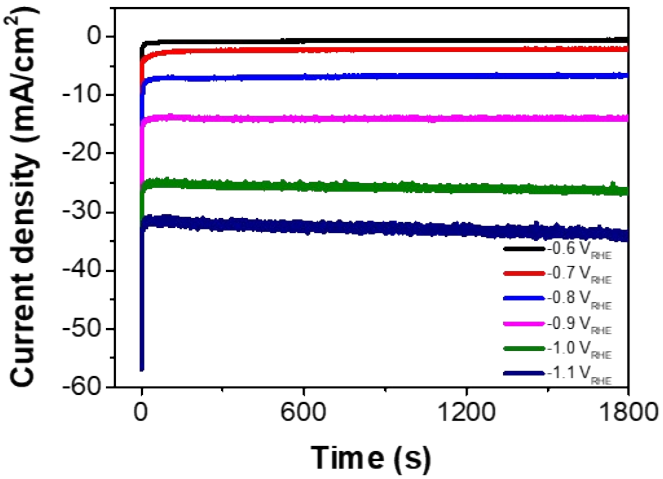

Figure S11. CA curves during FE measurements.

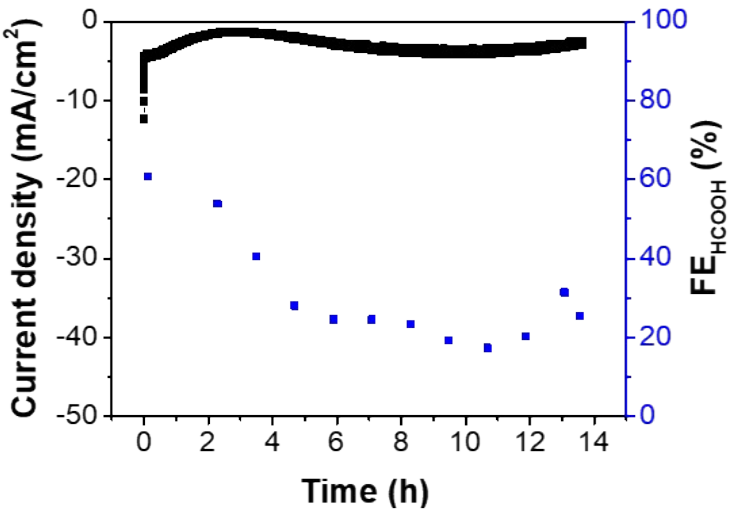

Figure S12. FE_{HCOOH} and CA curve of Bi film.

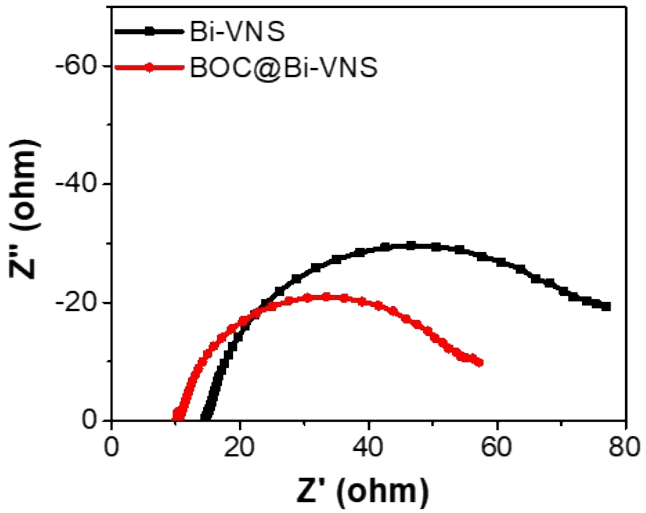

Figure S13. Nyquist plots for Bi-VNS and BOC@Bi-VNS.

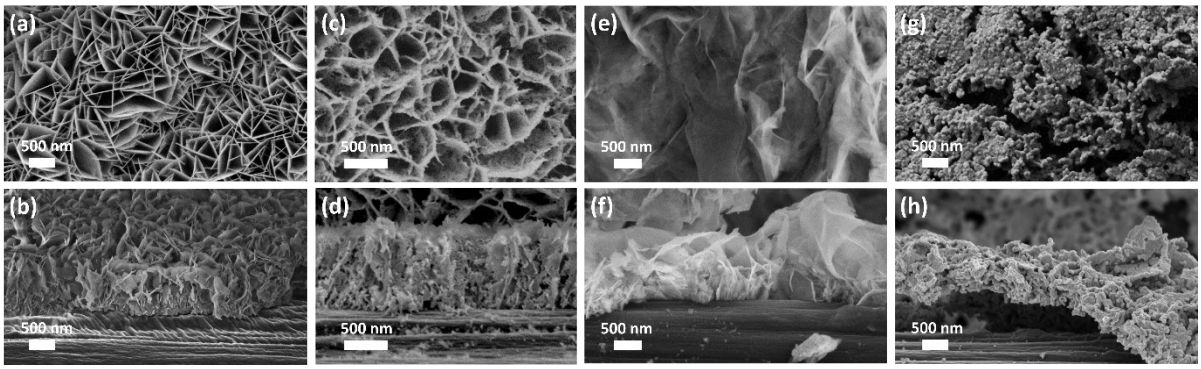

Figure S14. Top-view and cross-sectional view SEM images of Bi-based cathodes at each stage. (a,b) BiOI, (c,d) Bi-VNS, (e,f) Bi-VNS after 12 h of electrolysis, (g,h) Bi-VNS after 24 h of electrolysis (BOC@Bi-VNS).

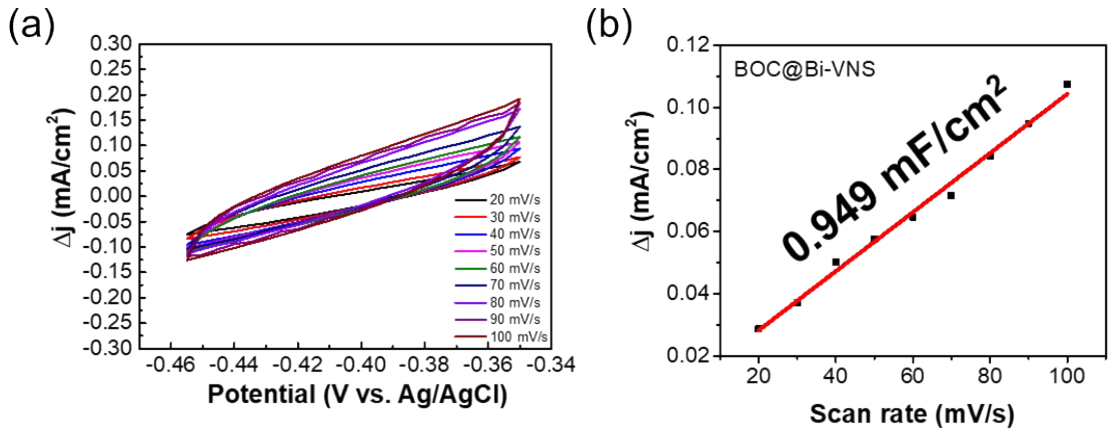

Figure S15. (a) CV curves at different scan rates and (b) calculated double-layer capacitances (C_{DL}) of BOC@Bi-VNS.

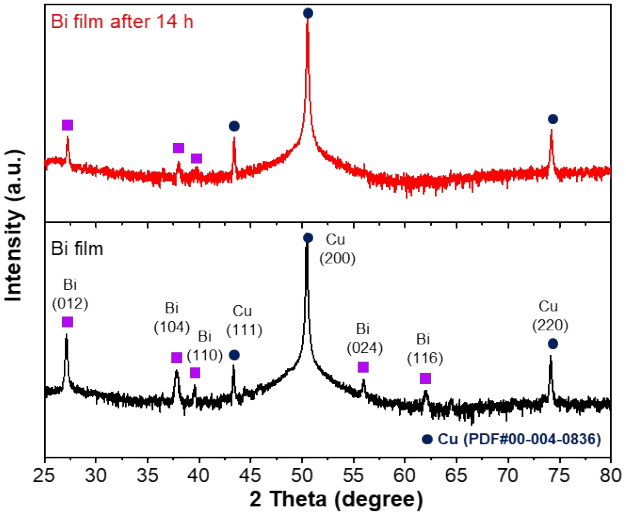

Figure S16. XRD patterns of Bi films.

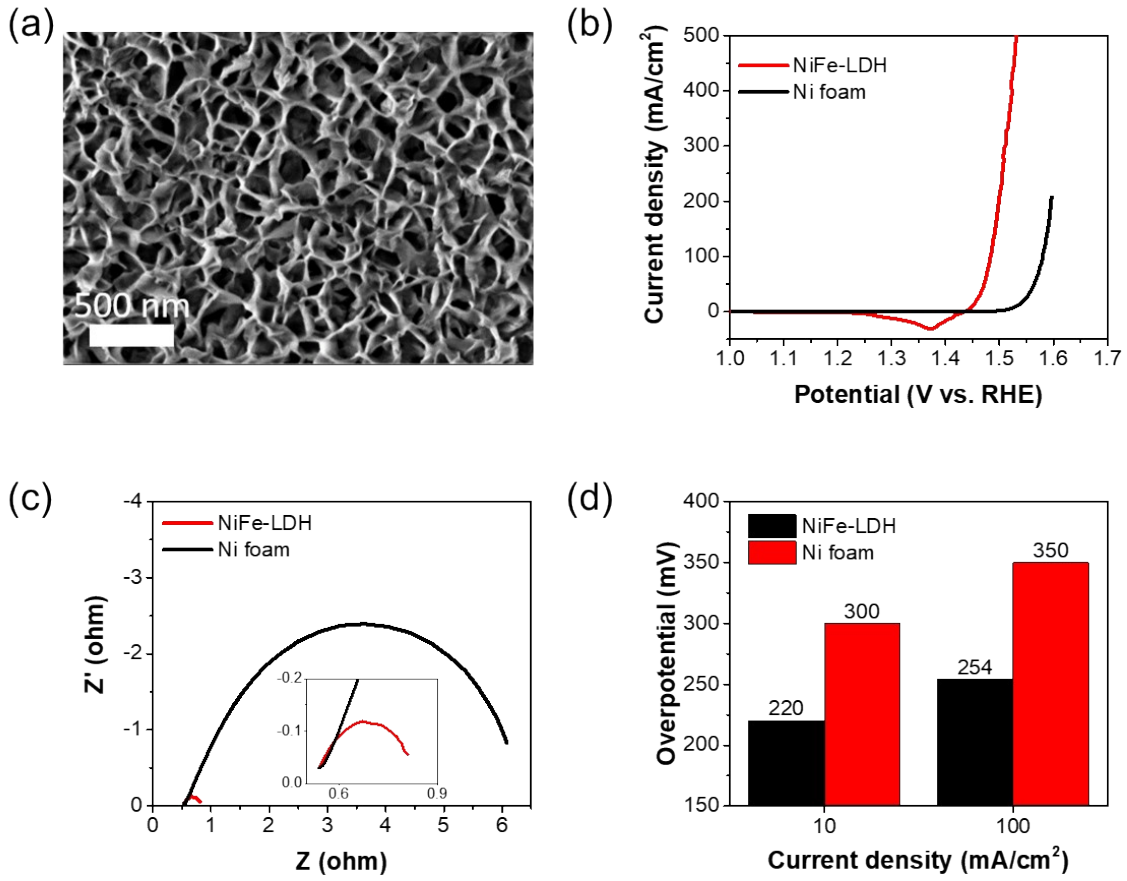

Figure S17. (a) SEM image of NiFe-LDH. (b) LSV, (c) Nyquist plots (inset: magnified plots) and (d) overpotentials of NiFe-LDH and Ni foam

Table S1. Faradaic efficiencies and partial current densities for CO_2RR electrocatalysts in a gas-tight H-cell.

Materials	Electrolyte	$FE_{HCOOH, MAX}$ (%)	j_{HCOOH} at FE_{MAX} (mA cm^{-2})	Potential (V vs. RHE)	Ref.
Bi-VNS	0.2 M $KHCO_3$	97.2	32.5	-1.1	This Work
BMNS	0.5 M $KHCO_3$	98	23	-0.8	1
Cu foam@BiNW	0.5 M $NaHCO_3$	95	15	-0.69	2
Bi nanosheets	0.1 M $KHCO_3$	86	16.5	-1.1	3
Bi-NRs@NCNT	0.1 M $KHCO_3$	90.9	≈5	-0.9	4
Bi NR	0.5 M $KHCO_3$	98.6	≈5	-0.8	5
Bi@Sn NPs	0.5 M $KHCO_3$	91	31	-1.1	6
Bi19Br3S27	0.1 M $KHCO_3$	98	N/A	-1.1	7
D-NR	0.5 M $KHCO_3$	81.3	≈7	-1	8
Bi-Sn	0.1 M $KHCO_3$	93.9	9.3	-1	9
MHKTs	0.5 M $KHCO_3$	95	< 1	-1	10
NiSn-APC nanoarray	0.5 M $KHCO_3$	86.1	20.8	-0.82	11
SL-NG@Sn foil	0.5 M $KHCO_3$	92	21.3	-1	12
CuSn NPs	0.5 M $KHCO_3$	53	N/A	-1	13
Cu70Sn30	0.5 M $KHCO_3$	90	N/A	-1.1	14
Ag75/(A-Sn(IV))25	0.5 M $NaHCO_3$	75.1	13.4	-0.9	15
Sn-MOF	0.5 M $KHCO_3$	92	23.2	-1.2	16

Table S2. R_{ct} values of each sample

	R_{ct} (Ω)
Bi film	388.2
Bi-VNS	68.74
BOC@Bi-VNS	48.09

Table S3. Comparison of the performances of reported solar-driven systems using cost-effective PV cells.

Materials	System type	Main reaction product	FE_{MAX} of the Product (%)	STF (%)	Stability (h)	Year	Ref.
Bi-VNS	PV-EC	HCOOH	97.2	11.5	13	2023	This work
BOI-Bi	PV-PEC	HCOOH	96.5	8.3	1	2021	[17]
Ti cathodes	PV-EC	HCOOH	80	7.2	5	2021	[18]
In/Cu mesh	PV-EC	HCOOH	67	1.8	1.5	2014	[19]
Sn/Cu	PV-EC	HCOOH	65	5.7	N/A	2022	[20]
$Bi_{19}Br_3S_{27}$	PV-EC	HCOOH	98	4.75	3	2023	[7]
nano-Ag	PV-EC	CO	93	8.05	8	2020	[21]
Au	PV-EC	CO	≈90	7	18	2015	[22]
np-Ag	PV-EC	CO	78.1	≈6.5	2	2017	[23]
Au/CdTe/ZnTe	PV-PEC	CO	≈80	0.43	3	2016	[24]
GB-Cu	PV-EC	C2H4	38	3.88	~3	2020	[25]
Cu-Zn	monolithic PV-EC	Syngas	85	4.3	3	2017	[26]
CuAg	PV-EC	Hydrocarbons & oxygenates	30-40	3.8	6	2017	[27]

REFERENCE

1. Li, N.; Yan, P.; Tang, Y.; Wang, J.; Yu, X.-Y.; Wu, H. Bin. In-Situ Formation of Ligand-Stabilized Bismuth Nanosheets for Efficient CO2 Conversion. *Appl. Catal. B* **2021**, *297*, 120481.

2. Zhang, X.; Sun, X.; Guo, S.-X.; Bond, A. M.; Zhang, J. Formation of Lattice-Dislocated Bismuth Nanowires on Copper Foam for Enhanced Electrocatalytic CO2 Reduction at Low Overpotential. *Energy Environ. Sci.* **2019**, *12* (4), 1334–1340.

3. Zhang, W.; Hu, Y.; Ma, L.; Zhu, G.; Zhao, P.; Xue, X.; Chen, R.; Yang, S.; Ma, J.; Liu, J.; Jin, Z. Liquid-Phase Exfoliated Ultrathin Bi Nanosheets: Uncovering the Origins of Enhanced Electrocatalytic CO2 Reduction on Two-Dimensional Metal Nanostructure. *Nano Energy* **2018**, *53*, 808–816.

4. Zhang, W.; Yang, S.; Jiang, M.; Hu, Y.; Hu, C.; Zhang, X.; Jin, Z. Nanocapillarity and Nanoconfinement Effects of Pipet-like Bismuth@Carbon Nanotubes for Highly Efficient Electrocatalytic CO2 Reduction. *Nano Lett.* **2021**, *21* (6), 2650–2657.

5. Li, Y.; Chen, J.; Chen, S.; Liao, X.; Zhao, T.; Cheng, F.; Wang, H. In Situ Confined Growth of Bismuth Nanoribbons with Active and Robust Edge Sites for Boosted CO2 Electroreduction. *ACS Energy Lett.* **2022**, *7* (4), 1454–1461.

6. Xing, Y.; Kong, X.; Guo, X.; Liu, Y.; Li, Q.; Zhang, Y.; Sheng, Y.; Yang, X.; Geng, Z.; Zeng, J. Bi@Sn Core–Shell Structure with Compressive Strain Boosts the Electroreduction of CO2 into Formic Acid. *Adv. Sci.* **2020**, *7* (22), 1902989.

7. Ma, X.; Wang, Q.; Wang, M.; Jin, X.; Wang, L.; Zhang, L. Bi19Br3S27 Nanorods for Formate Production from CO2 Electroreduction with High Efficiency and Selectivity. *Chem. Eng. J.* **2023**, *474*, 145711.

8. Xu, J.; Yang, S.; Ji, L.; Mao, J.; Zhang, W.; Zheng, X.; Fu, H.; Yuan, M.; Yang, C.; Chen, H.; Li, R. High Current CO2 Reduction Realized by Edge/Defect-Rich Bismuth Nanosheets. *Nano Res.* **2023**, *16* (1), 53–61.

9. Wu, Z.; Wu, H.; Cai, W.; Wen, Z.; Jia, B.; Wang, L.; Jin, W.; Ma, T. Engineering Bismuth–Tin Interface in Bimetallic Aerogel with a 3D Porous Structure for Highly Selective Electrocatalytic CO2 Reduction to HCOOH. *Angew. Chem. Int. Ed.* **2021**, *60* (22), 12554–12559.

10. Huang, J.; Guo, X.; Huang, X.; Wang, L. Metal (Sn, Bi, Pb, Cd) in-Situ Anchored on Mesoporous Hollow Kapok-Tubes for Outstanding Electrocatalytic CO2 Reduction to Formate. *Electrochim. Acta* **2019**, *325*, 134923.

11. Xie, W.; Li, H.; Cui, G.; Li, J.; Song, Y.; Li, S.; Zhang, X.; Lee, J. Y.; Shao, M.; Wei, M. NiSn Atomic Pair on an Integrated Electrode for Synergistic Electrocatalytic CO2 Reduction. *Angew. Chem. Int. Ed.* **2021**, *60* (13), 7382–7388.

12. Huang, J.; Guo, X.; Wei, Y.; Hu, Q.; Yu, X.; Wang, L. A Renewable, Flexible and Robust Single Layer Nitrogen-Doped Graphene Coating Sn Foil for Boosting Formate Production from Electrocatalytic CO2 Reduction. *J. CO2 Util.* **2019**, *33*, 166–170.

13. Xiong, W.; Yang, J.; Shuai, L.; Hou, Y.; Qiu, M.; Li, X.; Leung, M. K. H. CuSn Alloy Nanoparticles on Nitrogen-Doped Graphene for Electrocatalytic CO2 Reduction. *ChemElectroChem* **2019**, *6* (24), 5951–5957.

14. Ren, W.; Tan, X.; Qu, J.; Li, S.; Li, J.; Liu, X.; Ringer, S. P.; Cairney, J. M.; Wang, K.; Smith, S. C.; Zhao, C. Isolated Copper–Tin Atomic Interfaces Tuning Electrocatalytic CO2 Conversion. *Nat. Commun.* **2021**, *12* (1), 1449.

15. Zhang, J.; Qiao, M.; Li, Y.; Shao, Q.; Huang, X. Highly Active and Selective Electrocatalytic CO2 Conversion Enabled by Core/Shell Ag/(Amorphous-Sn(IV)) Nanostructures with Tunable Shell

Thickness. *ACS Appl. Mater. Interfaces* **2019**, *11* (43), 39722–39727.

16. Wang, X.; Zou, Y.; Zhang, Y.; Marchetti, B.; Liu, Y.; Yi, J.; Zhou, X.-D.; Zhang, J. Tin-Based Metal Organic Framework Catalysts for High-Efficiency Electrocatalytic CO2 Conversion into Formate. *J. Colloid Interface Sci.* **2022**, *626*, 836–847.

17. Zhao, J.; Xue, L.; Niu, Z.; Huang, L.; Hou, Y.; Zhang, Z.; Yuan, R.; Ding, Z.; Fu, X.; Lu, X.; Long, J. Conversion of CO2 to Formic Acid by Integrated All-Solar-Driven Artificial Photosynthetic System. *J. Power Sources* **2021**, *512*, 230532.

18. Kato, N.; Mizuno, S.; Shiozawa, M.; Nojiri, N.; Kawai, Y.; Fukumoto, K.; Morikawa, T.; Takeda, Y. A Large-Sized Cell for Solar-Driven CO2 Conversion with a Solar-to-Formate Conversion Efficiency of 7.2%. *Joule* **2021**, *5* (3), 687–705.

19. White, J. L.; Herb, J. T.; Kaczur, J. J.; Majsztrik, P. W.; Bocarsly, A. B. Photons to Formate: Efficient Electrochemical Solar Energy Conversion via Reduction of Carbon Dioxide. *J. CO2 Util.* **2014**, *7*, 1–5.

20. Thijs, B.; Hanssens, L.; Heremans, G.; Wangermez, W.; Rongé, J.; Martens, J. A. Demonstration of a Three Compartment Solar Electrolyser with Gas Phase Cathode Producing Formic Acid from CO2 and Water Using Earth Abundant Metals. *Front. Chem. Eng.* 2022.

21. Chae, S. Y.; Lee, S. Y.; Han, S. G.; Kim, H.; Ko, J.; Park, S.; Joo, O.-S.; Kim, D.; Kang, Y.; Lee, U.; Hwang, Y. J.; Min, B. K. A Perspective on Practical Solar to Carbon Monoxide Production Devices with Economic Evaluation. *Sustain. Energy Fuels* **2020**, *4* (1), 199–212.

22. Schreier, M.; Curvat, L.; Giordano, F.; Steier, L.; Abate, A.; Zakeeruddin, S. M.; Luo, J.; Mayer, M. T.; Grätzel, M. Efficient Photosynthesis of Carbon Monoxide from CO2 Using Perovskite Photovoltaics. *Nat. Commun.* **2015**, *6* (1), 7326.

23. Sriramagiri, G. M.; Ahmed, N.; Luc, W.; Dobson, K. D.; Hegedus, S. S.; Jiao, F. Toward a Practical Solar-Driven CO2 Flow Cell Electrolyzer: Design and Optimization. *ACS Sustain. Chem. Eng.* **2017**, *5* (11), 10959–10966.

24. Jang, Y. J.; Jeong, I.; Lee, J.; Lee, J.; Ko, M. J.; Lee, J. S. Unbiased Sunlight-Driven Artificial Photosynthesis of Carbon Monoxide from CO2 Using a ZnTe-Based Photocathode and a Perovskite Solar Cell in Tandem. *ACS Nano* **2016**, *10* (7), 6980–6987.

25. Chen, Z.; Wang, T.; Liu, B.; Cheng, D.; Hu, C.; Zhang, G.; Zhu, W.; Wang, H.; Zhao, Z.-J.; Gong, J. Grain-Boundary-Rich Copper for Efficient Solar-Driven Electrochemical CO2 Reduction to Ethylene and Ethanol. *J. Am. Chem. Soc.* **2020**, *142* (15), 6878–6883.

26. Urbain, F.; Tang, P.; Carretero, N. M.; Andreu, T.; Gerling, L. G.; Voz, C.; Arbiol, J.; Morante, J. R. A Prototype Reactor for Highly Selective Solar-Driven CO2 Reduction to Synthesis Gas Using Nanosized Earth-Abundant Catalysts and Silicon Photovoltaics. *Energy Environ. Sci.* **2017**, *10* (10), 2256–2266.

27. Gurudayal; Bullock, J.; Srankó, D. F.; Towle, C. M.; Lum, Y.; Hettick, M.; Scott, M. C.; Javey, A.; Ager, J. Efficient Solar-Driven Electrochemical CO2 Reduction to Hydrocarbons and Oxygenates. *Energy Environ. Sci.* **2017**, *10* (10), 2222–2230.